Spatial-spectral coupling in coherent anti-Stokes Raman scattering microscopy

Aaron M. Barlow,[1,2,*] **Konstantin Popov,**[1,4] **Marco Andreana,**[1,2] **Douglas J. Moffatt,**[2] **Andrew Ridsdale,**[2] **Aaron D. Slepkov,**[3] **James L. Harden,**[1] **Lora Ramunno,**[1] **and Albert Stolow**[1,2]

[1]*Department of Physics, University of Ottawa, Ottawa ON, Canada*
[2]*SDT, Emerging Technologies Division, National Research Council of Canada, 100 Sussex Dr., Ottawa ON, Canada*
[3]*Department of Physics & Astronomy, Trent University, Peterborough ON, Canada*
[4]*kpopov@uottawa.ca*
[*]*abarlow@uottawa.ca*

Abstract: Coherent anti-Stokes Raman scattering (CARS) microscopy is a third-order nonlinear optical technique which permits label-free, molecule-specific hyperspectral imaging. The interference between coherent resonant and non-resonant terms leads to well known distortions in the vibrational spectrum, requiring the use of retrieval algorithms. It also leads to spatial imaging distortions, largely due to the Gouy phase, when objects are smaller than the Rayleigh range. Here we consider that the focal position and spectral contributions to the nonlinear image formation are intrinsically coupled and cannot be corrected by conventional retrieval methods.

OCIS codes: (020.3690) Line shapes and shifts; (030.1670) Coherent optical effects; (180.4315) Nonlinear microscopy; (300.6230) Spectroscopy, coherent anti-Stokes Raman scattering.

References and links

1. A. Zumbusch, G. R. Holtom, and X. S. Xie, "Three-dimensional vibrational imaging by coherent anti-Stokes Raman scattering," Phys. Rev. Lett. **82** 4142–4145 (1999).
2. E. O. Potma and X. S. Xie, "CARS microscopy for biology and medicine," Opt. Photon. News **15**, 40–45 (2004).
3. C. L. Evans and X. S. Xie, "Coherent anti-Stokes Raman scattering microscopy: chemical imaging for biology and medicine," Annu. Rev. Anal. Chem. **1**, 883–909 (2008).
4. J. Cheng, A. Volkmer, L. D. Book, and X. S. Xie, "An epi-detected coherent anti-Stokes Raman scattering (E-CARS) microscope with high spectral resolution and high sensitivity," J. Phys. Chem. B **105**, 1277–1280 (2001).
5. L. Li, H. Wang, and J. Cheng, "Quantitative coherent anti-Stokes Raman scattering imaging of lipid distribution in coexisting domains", Biophys. J. **89**, 3480–3490 (2005).
6. M. Müller and J. M. Schins, "Imaging the thermodynamic state of lipid membranes with multiplex CARS microscopy," J. Phys. Chem. **106**, 3715–3723 (2002).
7. S. H. Parekh, Y. J. Lee, K. A. Aamer and M. T. Cicerone, "Label-free cellular imaging by broadband coherent anti-Stokes Raman scattering microscopy," Biophys. J. **99**, 2695–2704 (2010).
8. A. F. Pegoraro, A. D. Slepkov, A. Ridsdale, D. J. Moffatt, and A. Stolow, "Hyperspectral multimodal CARS microscopy in the fingerprint region," J. Biophotonics DOI 10.1002/jbio.201200171 (2012)
9. C. Chung, J. Hsu, S. Mukamel, and E. O. Potma, "Controlling stimulated coherent spectroscopy and microscopy by a position-dependent phase," Phys. Rev. A **87**, 033833 (2013).
10. S. Maeda, T. Kamisuki, and Y. Adachi, *Advances in Non-linear Spectroscopy*, R. J. H. Clark and R. E. Hester, eds. (John Wiley and Sons Ltd., 1988) p. 253.
11. E. O. Potma, C. L. Evans, and X. S. Xie, "Heterodyne coherent anti-Stokes Raman scattering (CARS) imaging," Opt. Lett. **31**, 241–243 (2006).

#189626 - $15.00 USD Received 30 Apr 2013; revised 7 Jun 2013; accepted 9 Jun 2013; published 19 Jun 2013

12. W. M. Tolles, J. W. Nibler, J. R. McDonald, and A. B. Harvey, "A Review of the Theory and Applications of Coherent Anti-Stokes Raman Spectroscopy (CARS)," Appl. Spectrosc. 31 253–271 (1971).
13. Y. Liu, Y. J. Lee, and M. T. Cicerone, "Broadband CARS spectral phase retrieval using a time-domain Kramers-Kronig transform," Opt. Lett. **34**, 1363–1365 (2009).
14. E. M. Vartiainen, H. A. Rinia, M. Müller, and M. Bonn, "Direct extraction of Raman line-shapes from congested CARS spectra," Opt. Express **14**, 3622–3630 (2006).
15. G. L. Eesley, *Coherent Raman Spectroscopy* (Pergamon Press, 1981).
16. E. O. Potma, W. P. de Boeij, and D. A. Wiersma, "Nonlinear coherent four-wave mixing in optical microscopy," J. Opt. Soc. Am. B **17**, 1678–1684, (2000).
17. J. Cheng, A. Volkmer, and X. S. Xie, "Theoretical and experimental characterization of coherent anti-Stokes Raman scattering microscopy," J. Opt. Soc. Am. B **19**, 1363–1375 (2002).
18. N. Djaker, D. Gachet, N. Sandeau, PF. Lenne, and H. Rigneault, "Refractive effects in coherent anti-Stokes Raman scattering microscopy," Appl. Opt. **45**, 7005-7011 (2006).
19. K. I. Popov, A. F. Pegoraro, A. Stolow, and L. Ramunno, "Image formation in CARS microscopy: effect of the Gouy phase shift," Opt. Express **19**, 5902–5911 (2011).
20. D. Gachet, F. Billard, N. Sandeau and H. Rigneault, "Coherent anti-Stokes Raman scattering (CARS) microscopy imaging at interfaces: evidence of interference effects," Opt. Express **15** 10408–10420 (2007).
21. D. Gachet, F. Billard, and H. Rigneault, "Focused field symmetries for background-free coherent anti-Stokes Raman spectroscopy," Phys. Rev. A **77** 061802(R) 1–4 (2008).
22. D. Gachet, S. Brustlein, and H. Rigneault, "Revisiting the Youngs double slit experiment for background-free nonlinear Raman spectroscopy and microscopy," Phys. Rev. Lett. **104** 213905 1–4 (2010).
23. C. V. Stephenson, W. C. Coburn Jr., and W. S. Wilcox, "The vibrational spectra and assignments of nitrobenzene, phenyl isocyanate, phenyl isothiocyanate, thionylaniline and anisole", Spectrochim. Acta **17**, 933–946 (1961).
24. A. F. Pegoraro, A. Ridsdale, D. J. Moffatt, Y. Jia, J. P. Pezacki and A. Stolow, "Optimally chirped multimodal CARS microscopy based on a single Ti:sapphire oscillator," œ**17** 2984–2996 (2009).
25. K. S. Yee, "Numerical solution of initial boundary value problems involving maxwell's equations in isotropic media ," IEEE Trans. Ant. Prop. **14**, 302–307 (1966).
26. M. Fujii, M. Tahara, I. Sakagami, W. Freude, and P. Russer, "High-order FDTD and auxiliary differential equation formulation of optical pulse propagation in 2-D Kerr and Raman nonlinear dispersive media," IEEE J. Quant. Electron. **40**, 175–182 (2004).
27. D. Vanderbilt and S. G. Louie, "A Monte Carlo simulated annealing approach to optimization over continuous variables," J. Comput. Phys. **56**, 259–271 (1984).

1. Introduction

As nonlinear optics continues to impact biophysics and biomedical imaging, understanding the physics of the image formation process takes on increasing importance. A notable example is coherent anti-Stokes Raman scattering (CARS) microscopy, a label-free, molecule-specific third-order nonlinear optical imaging method wherein contrast is achieved via vibrational Raman resonances [1–4]. As molecular vibrations are sensitive to the chemical, physical, or thermodynamic state of a system, the most detailed information results from the spatial variation of the Raman spectrum across the sample: this is known as hyperspectral CARS imaging [5–8]. In general, the physics of nonlinear optical image formation is more complex than that of linear microscopies. Here we show that spatial and spectral contributions to the nonlinear image formation are intrinsically coupled. Although we discuss the specific case of CARS microscopy, our results apply more generally to resonant nonlinear microscopies, including stimulated Raman scattering [9].

The analysis of CARS spectra is complicated by coherent interaction of the resonant signal with the non-resonant background (NRB) signal due to electronic four-wave mixing within the sample [10]. The NRB signal can overwhelm the resonant signal in cases where the concentration of resonant oscillators is low [11], particularly when the resonant object is small compared to the Rayleigh range. The frequency dependence of the phase shift $\varphi(\omega)$ of the resonant response relative to that of the NRB leads to well known spectral distortions [12]. Hyperspectral CARS imaging has dealt with this via the application of phase retrieval algorithms [13, 14] which decouple the resonant and non-resonant source terms in the third-order nonlinear susceptibility $\chi^{(3)}(\omega)$. It is commonly assumed that the CARS signal intensity is proportional to

#189626 - $15.00 USD Received 30 Apr 2013; revised 7 Jun 2013; accepted 9 Jun 2013; published 19 Jun 2013

the squared modulus of the third order non-linear susceptibility $\chi^{(3)}(\omega)$ as follows [15]

$$I_{CARS}(\omega) \propto |\chi^{(3)}(\omega)|^2 = |\chi^{(3)}_{NR} + \chi^{(3)}_{R}(\omega)|^2, \quad (1)$$

where $\chi^{(3)}_{R}$ and $\chi^{(3)}_{NR}$ are the resonant and non-resonant (i.e. imaginary and real) components of $\chi^{(3)}(\omega)$. Having measured $|\chi^{(3)}(\omega)|$ using Eq. (1), one can deduce the spectral phase $\varphi(\omega)$—defined by $\chi^{(3)}(\omega) = |\chi^{(3)}(\omega)| \exp(i\varphi(\omega))$—using the general properties of the susceptibility, and use this to retrieve the purely imaginary (i.e. resonant) response as discussed, for example, in Ref. [13]. After such methods are applied, the resulting spectrum should be identical to the spontaneous Raman spectrum of the sample, provided that the retrieval algorithm uses an accurate model to describe the spectral phase in the system. This procedure is expected to show the form and location of the physical object, whereas any spatial variation in the retrieved Raman spectrum associated with the object is expected to relate to local chemical or thermodynamic changes in the sample.

The coherent interaction of resonant and NRB terms also leads to spatial distortions. In particular, the third order polarization from micron-sized objects typically reveals asymmetric "shadows" which extend for several microns beyond their physical length, in the axial (propagation) direction. These have been been interpreted as being due to destructive interference in the coherent signal [16, 17] arising from effects such as the linear index mismatch between the emitter and the surrounding medium [18]. Recently, it was demonstrated that for objects smaller than the Rayleigh range of the laser focus, there are asymmetric distortions in the signal intensity which depend on the position of the object within the focus and that these distortions can be attributed to interference arising from the Gouy phase shift of the resonant object relative to that of the nonresonant background [19]. Moreover, in the spectral domain, it was established that the Gouy phase shift [20, 21] and linear index mismatch [22] may introduce spectral shifts at interfaces between resonant and non-resonant media. Here, we examine the situation where spectral distortions result from a small resonator embedded in a nonresonant medium in the realistic situation (i) where the resonant and NRB responses are comparable and (ii) the sample contains spatial inhomogeneities on the scale of the Rayleigh range. We find that the Gouy phase shift leads to significant distortions in the CARS spectrum, and that similar distortions are also found to occur as a result of linear index mismatch between the emitter and medium. We further demonstrate that simple phase retrieval algorithms will yield a spectrally distorted Raman spectrum and that these distortions are dependent on the position of the object within the focus, even for objects of uniform composition. We emphasize that awareness of the intrinsic nature of spatial-spectral coupling in CARS microscopy is required in order to obtain faithful hyperspectral images of complex biological systems.

In order to demonstrate the effects of the spatial-spectral coupling in CARS microscopy, we conducted a series of CARS hyperspectral imaging experiments using a prototypical sample: a small resonant droplet embedded in a non-resonant medium, as described in Section 2. In Section 3, we present detailed numerical simulations of this physical situation. In Section 4, we analyse the revealed spatial-spectral coupling and subsequent retrievals of the Raman spectra. In Section 5, we summarize our results.

2. Experimental observations

In order to generate chemically uniform samples of suitable size embedded in a non-resonant background medium, we made an emulsion of approximately 1 part in 25 of nitrobenzene (NB) in 1% agarose via vigorous stirring at 80^{o}C. A drop of this emulsion was placed between a coverslip and slide and allowed to gel in order to distribute nitrobenzene droplets of sizes $\sim$1 μm to $\sim$10 μm, as highlighted in Fig. 1. NB has several Raman resonances in the fingerprint

#189626 - $15.00 USD Received 30 Apr 2013; revised 7 Jun 2013; accepted 9 Jun 2013; published 19 Jun 2013

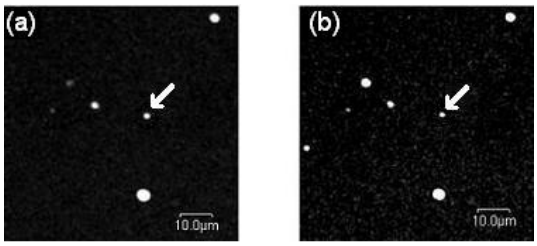

Fig. 1. CARS microscopy of small nitrobenzene droplets of various sizes in agarose gel medium, imaged at Raman shifts of 1580 cm^{-1}. (a) A CARS image recorded at the best focus ($z = 0$ μm) for the highlighted droplet. (b) A CARS image of the identical droplets, but with the focus displaced to $z = -1$ μm with respect to that in panel (a). Importantly, the Raman retrieved Raman spectra associated with these focal positions are different, as seen in Fig. 2.

region, including a weak C=C stretch mode at 1585 cm^{-1} [23]. This resonance was selected, as we expect the interference effect to be maximized for a weak Raman resonance. The agarose gel is sufficiently dilute that it does not contribute to the resonant response, and the measured response from the gel yielded an essentially a flat NRB. Using the single femtosecond oscillator, chirped pulse configuration described in Ref. [8], we recorded hyperspectral CARS images in the fingerprint region—from $\sim$1000 cm^{-1} to $\sim$1800 cm^{-1}—using laser powers of 180 mW and 20 mW for pump and Stokes, respectively, measured at the input to the microscope scan head. The Raman spectral resolution was $\sim$30 cm^{-1}, determined by the selected linear chirp [24]. The spectrum was calibrated by direct measurement of the pump anti-Stokes wavelengths using a spectrometer and correlating its frequency to the position on the translation stage.

Within the field of view, we located an isolated NB droplet of size $\sim$1 μm, shown in Fig. 1(a), and recorded CARS spectra as a function of z displacement, using 0.5 μm steps in z ranging from -2.5 μm to +2.5 μm from the centre of the highlighted droplet. Negative z corresponds to the NB droplet's position being closer to the laser source. In Fig. 1(a), we show the highlighted NB droplet imaged at the best focus position, defined to be z = 0 μm. For comparison, in Fig. 1(b), we show the identical NB droplet but with the focus displaced to z = -1 μm.

The raw CARS spectrum of NB obtained from the droplet located at z = 0 μm is shown as open circles in Fig. 2(a). The CARS spectrum displays the expected red-shift of its maximum due to the interference between the resonant and NRB contributions [3]. The CARS spectra of the NB droplet at z = -1 μm and z = 1 μm focus are also shown in Fig. 2(a). Despite the CARS images in Figs. 1(a) and 1(b) appearing nearly identical, the raw CARS spectra are considerably different. We observed distortions of the spectral amplitude and position of the peak and dip, even though magnitudes of the resonant and non-resonant signals should be approximately the same in each case (since the NB droplet is entirely within the Rayleigh range for all three cases). In Fig. 2(b), we show the Raman spectra at each focus position, retrieved using an established Kramers-Kronig algorithm [13]. The retrieved spectrum at z = 0 is consistent with the high resolution spontaneous Raman spectrum (solid line), albeit at our lower spectral resolution of $\sim$30 cm^{-1}. However, it can be seen that displacing the focus from z = -1 μm to z = +1 μm causes a spectral shift in the maximum of order $\sim$10 cm^{-1}.

3. Numerical simulations

In order to illuminate these experimental results, we performed 3D numerical simulations using a finite-difference time-domain (FDTD) procedure [19]. An electromagnetic source composed of the sum of tightly focused (NA = 1) pump and Stokes beams was excited at the boundary of

#189626 - $15.00 USD Received 30 Apr 2013; revised 7 Jun 2013; accepted 9 Jun 2013; published 19 Jun 2013

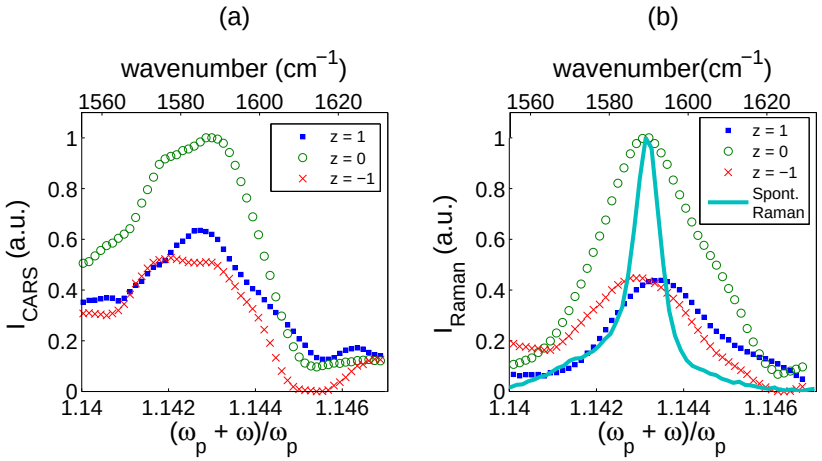

Fig. 2. (a) Experimentally measured raw CARS spectra of the highlighted NB droplet of Fig. 1, located at the z = 0 μm best focus position (circles) and at displaced foci (z = -1 μm, crosses, and z = +1 μm, squares). (b) The Raman spectra, retrieved via a Kramers-Kronig algorithm, of the same droplet, overlaid with the spontaneous Raman spectrum of NB (solid line). The intrinsic spatial-spectral coupling can be seen from the z-dependence of the retrieved Raman spectrum, in this case, the peak maximum varying by $\sim$10 cm^{-1}. (Color online)

a cuboid simulation domain. The pump was assumed to have 0.9 μm wavelength in free space and the Stokes was down-shifted from the pump by a frequency ω. Both laser beam components were assumed to be 2 ps in duration. Inside the simulation domain, the electromagnetic wave was propagated numerically by the standard Maxwell solver [25]. The effect of the medium was accounted for by the proper constitutive relations in the Maxwell equations. The medium was assumed to have refraction index $n_0 = 1.34$ and possessed a nonzero Kerr nonlinear susceptibility which generated the NRB signal. The Raman medium response was described by the third-order Raman polarization [26]. When the electromagnetic pulse reached the boundaries of the simulation domain, it was absorbed. Near the absorbing boundaries, the frequency components of the pulse, which also contained all the frequencies generated by the media including the anti-Stokes signal, were recorded and analytically propagated to the far-field zone where they were measured on the laser axis.

For a straightforward demonstration of spatial-spectral coupling in CARS microscopy, we assumed the NRB medium to be homogeneous throughout the simulation domain while the resonant Raman medium (NB droplet) was represented by a 1 μm-diameter spherical droplet located somewhere on the laser axis. The droplet could also have a linear refractive index generally different from that of the NRB (see below). The magnitudes of the nonlinear susceptibilities were chosen such that the strengths of the resulting NRB and resonant signals were comparable, as was the case for the experimental results presented above. The Raman resonant frequency Ω_R and line width Γ were chosen to be Ω_R = 1600 cm^{-1} (0.144 ω_p, where ω_p is the central frequency of the pump beam) and Γ = $\sim$15 cm^{-1} ($1.34 \times 10^{-3}\omega_p$).

We first consider the case of a micron-sized NB droplet which has a linear refractive index matched to that of the NRB. The simulation results for this case are plotted in Fig. 3(a). The

#189626 - $15.00 USD Received 30 Apr 2013; revised 7 Jun 2013; accepted 9 Jun 2013; published 19 Jun 2013

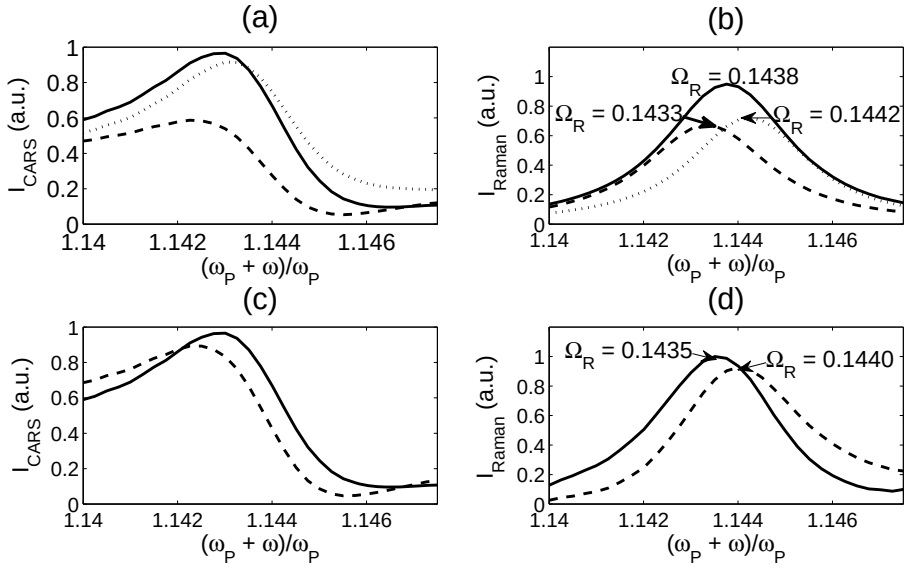

Fig. 3. Numerical (FDTD) simulations of spatial-spectral coupling in CARS microscopy. (a) CARS spectra of NB droplets in a uniform NRB, located at the z = 0 μm best focus position (solid line) and displaced along z ($z = -1\,\mu$m, dashed line, and $z = +1\,\mu$m, dotted line), centered at Ω_R = 1600 cm^{-1}. (b) The Raman spectra of NB droplets retrieved using a standard protocol which does not consider the Gouy phase. The shift in Ω_R is 10 cm^{-1} ($9 \times 10^{-4}\omega_P$). (c) The CARS spectra are also affected by linear index mismatches for a resonant NB droplet located at the z = 0 μm best focus position, within a uniform NRB occupying the entire Rayleigh range. The case of linear index-matching with the NRB is shown as the solid CARS spectrum. Using the known linear refractive index difference between NB and agarose leads to the dashed line CARS spectrum. (d) The retrieved Raman spectra of the preceding case, accounting for the index mismatch. In this case, the shift in Ω_R is 5.5 cm^{-1} ($5 \times 10^{-4}\omega_P$)

CARS spectra of the NB droplet vary as a function of z displacement in a manner very similar to the z variations seen in the experimental results in Fig. 2(a). The CARS spectrum of the NB droplet located 1 μm before the focus is different from the spectrum at 1 μm after the laser focus, despite the laser intensity being the same at these points. The retrieval of these spectra are shown in Fig. 3(b), yielding a spectral shift of order 10 cm^{-1} ($9 \times 10^{-4}\omega_P$). We see that even an idealized model having a Gaussian laser envelope shape, a flat NRB spectrum and a matched linear refractive index reproduces the experimentally observed spatial-spectral coupling effect. The idealized model does not, however, quantitatively reproduce the intensities of the experimental CARS spectra, particularly at z = +1 μm. We note that accurately fitting the intensity profile requires detailed knowledge of the point spread function, as well as explicit knowledge of the resonant-to-nonresonant background ratio. Fortunately, the phases of these fields are relatively insensitive to these parameters and, therefore, they have minimal effect on the observed spectral shifts.

If the linear index mismatch between 1% agarose ($n = 1.34$) and nitrobenzene ($n = 1.554$) is accounted for in our simulations, further distortions, as shown in Fig 3(c), of the CARS spectrum are found as compared to the index-matched case; its subsequent retrieval is shown in 3(d), where the solid line assumes matching of the linear refractive indices and the dashed

#189626 - $15.00 USD Received 30 Apr 2013; revised 7 Jun 2013; accepted 9 Jun 2013; published 19 Jun 2013

line includes the known differing linear refractive indices of NB and 1% agarose. Beyond the dominant effect of the Gouy phase, the presence of a linear refractive index mismatch within the sample leads to a further spectral shift of order 5.5 cm^{-1} ($5\times10^{-4}\omega_P$) at the point of best focus. A similar spectral shift is expected at positions $z=\pm1\mu m$ that will be cumulative with the effects due to the Gouy phase; this may be especially problematic in specific cases, as the shift due to the refractive index will depend heavily on the size and shape of the particular object being probed.

4. Discussion

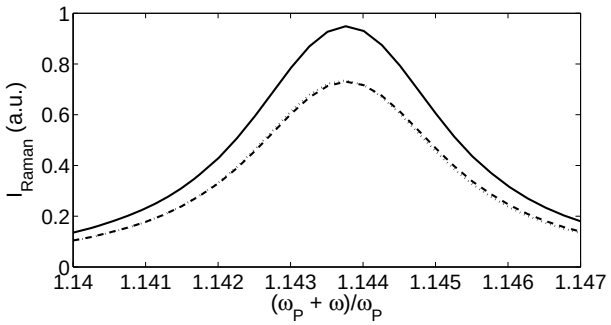

Fig. 4. Retrieved Raman spectra of NB droplet, using a modified algorithm which takes into account the effect of the Gouy phase. The retrieved spectra are for a droplet located at best focus (solid line) and displaced to $z=\pm\ 1\ \mu$m (dashed lines). These results show that including the intrinsic spatial-spectral coupling allows for accurate retrieval of the resonant Raman spectrum of sub-focal objects.

The experimental and simulation results are in excellent agreement, both in the qualitative effect and the quantitative magnitude of the spectral shift due to the change in position of the object within the Rayleigh range: there is a position-dependent spectral shift as the object moves axially through the focal plane. Importantly, the only physical quantity which changes due to displacements $z=\pm1\mu$m of the focal position in Fig. 2(a), or the correpsonding simulation in Fig. 3(a), is the Gouy phase shift of the laser beam. As was demonstrated in Ref. [19], the CARS response from wavelength-sized objects such as these NB droplets, or, more importantly, microscopic regions of physiological importance in biological samples, is affected by the local properties of the laser focus, including the Gouy phase shift. In general, the phase of the generated resonant CARS signal is shifted by $\delta\phi=2\phi_{Gp}-\phi_{Gs}+\delta\phi_l$, where ϕ_{Gp} and ϕ_{Gs} are the Gouy phase shifts of the pump and Stokes beams at the object location, respectively, and $\delta\phi_l$ is the extra phase shift due to any linear refractive index mismatches in the sample. Due to these additional propagation phase terms, the resonant response in Eq. (1) will no longer be purely imaginary. Rather, the following equation should be used to reveal these phases [21]

$$I_{CARS}(\omega)\propto|\chi^{(3)}(\omega)|^2=\left|\chi^{(3)}_{NR}+\chi^{(3)}_R(\omega)\mathbf{e}^{\mathbf{i}\delta\phi}\right|^2, \tag{2}$$

where the propagation phase $\delta\phi$ is written explicitly. More generally, this can be written as

$$|\chi^{(3)}(\omega)|^2=\left|\chi^{(3)}_{NR}+\frac{1}{V_R}\int_{V_R}\chi^{(3)}_R(\omega,\vec{r})e^{i\delta\phi(\vec{r})}d^3r\right|^2 \tag{3}$$

where V_R is the volume occupied by the resonant species. The $\delta\phi$ is a geometrical propagation factor and only varies slowly with ω over the range relevant to the CARS spectrum. After the

#189626 - $15.00 USD Received 30 Apr 2013; revised 7 Jun 2013; accepted 9 Jun 2013; published 19 Jun 2013

spatial integration is performed, Eq. (3) becomes equivalent to Eq. (2), yielding a certain phase $\delta\phi$ and magnitude of $\chi_R^{(3)}(\omega)$.

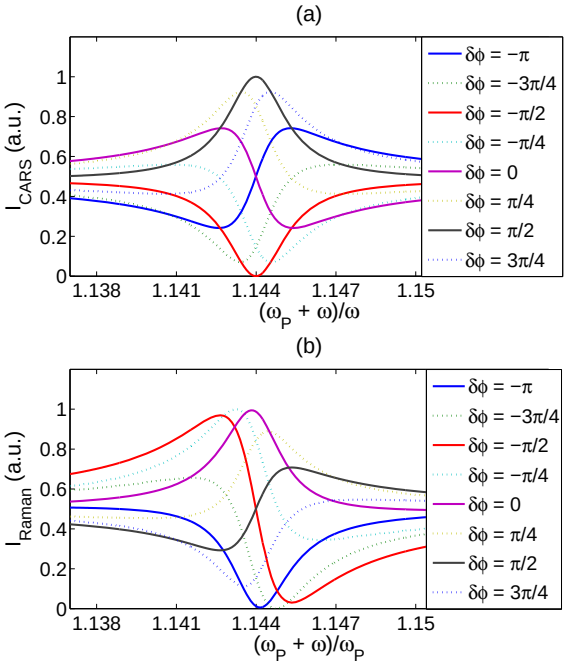

Fig. 5. The propagation phase term in Eq 2. has a significant effect on the form of both the CARS and retrieved Raman spectra. (a) Generated CARS spectra by assuming the Lorentzian line shape of Eq. (4), using the modified form of Eq.(2), for various $\delta\phi$. (b) The Raman retrieved spectra of the CARS lineshapes from (a). Use of standard retrieval algorithms can lead to significant distortions due to spatial-spectral coupling. (Color online)

If the phases contributing to $\delta\phi$ are known, the Raman spectrum can be generally retrieved from the CARS spectrum using Eq. (2). Development of a general retrieval routine which can provide this information is a challenging task and will be a subject for future studies. In the present case, we have specific *a priori* information about our simulated sample (i.e. there is only one isolated Raman line and an almost frequency-independent NRB) and, therefore, we can use a simple fitting procedure to retrieve the resonant Raman spectrum. Our fitting method is based on a simulated annealing search [27] for the least-squares global minimum. We fit the CARS spectra from Fig. 3(a) to the analytical expression in Eq. (2) with $\chi_R^{(3)}$ assumed to be a Lorentzian resonant shape of the form of Eq. (4).

$$\chi_R^{(3)}(\omega) = \chi_{R0}^{(3)} \frac{\Gamma}{\Omega_R - \omega - i\Gamma} \tag{4}$$

In Eq. (4), $\chi_{R0}^{(3)}$ is the constant amplitude (line strength) of the resonant susceptibility. By including $\delta\phi$ in the fit parameter space of the retrieval routine, the Raman spectrum can be reliably extracted as shown in Fig. 4, as can the phase shift information. Note that Fig. 3(b) is equivalent to the retrieved Raman spectrum using the explicit assumption of $\delta\phi = 0$, all other parameters ($\chi_{NR}^{(3)}$, $\chi_{R0}^{(3)}$, Ω_R, Γ) being fit by simulated annealing. This procedure (with

#189626 - $15.00 USD Received 30 Apr 2013; revised 7 Jun 2013; accepted 9 Jun 2013; published 19 Jun 2013

assumption $\delta\phi = 0$) corresponds to a retrieval procedure which does not include spatial-spectral coupling.

As seen from Eq. (2), the propagation phase term $\delta\phi$ results in the resonant term being no longer purely imaginary. Therefore, retrieval methods not accounting for this will generate an erroneous spectral phase $\varphi(\omega)$, leading to distortions in the retrieved Raman spectrum resulting from factors such as the Gouy phase shift or the linear refractive index mismatch within the sample. Importantly, this shows that the CARS spectrum is generally dependent on the internal composition of the inhomogeneous sample, even for objects of uniform chemical composition. It should be noted, however, that Eq. (2) can still be used without loss of generality for the retrieval of Raman data from the distorted CARS spectrum. From a phenomenological point of view, one can approximate the effects of $\delta\phi$ on the CARS spectral shape by substituting Eq. (4) directly into Eq. (2). This is shown in Fig. 5(a), where there is a family of CARS spectral line shapes, each corresponding to the same Raman line and the same relative amplitudes of resonant and nonresonant contributions to the CARS signal, but having a different phase $\delta\phi$. Upon retrieval of the Raman spectra using the standard Kramers-Kronig algorithm, shown in Fig. 5(b), we see that the expected simple resonant Raman lineshape is not retrieved, but rather we find a family of dispersive Raman peaks associated with the various phases. Due to the intrinsic nature of the coupling, post-processing images with Raman retrieval will be unable to reliably remove the spatial distortions (e.g. shadows) in the CARS image and may, in fact, introduce new artefacts leading to the possible misinterpretation of hyperspectral CARS images.

5. Conclusion

We have demonstrated that spectral line shape distortions in CARS microscopy are a function of the position of the object within the laser focus. By design, our NB droplet model system did not have any spatially varying chemical or thermodynamic properties which could result in any variation in the resonant Raman spectra. We emphasize that these observed and simulated spatial-spectral couplings are largely a geometric effect due to the Gouy phase shift between the resonant and non-resonant components of $\chi^{(3)}$, with contributions due to the linear index mismatch. Consequently, care must be taken in assigning physio-chemical significance to CARS spectral variations within samples having regions of interest smaller than the Rayleigh range of the laser focus. Such systems will invariably experience significant spatial-spectral coupling.

Spatial-spectral coupling effects can be safely neglected if one of two conditions are met. In the case where the $\chi_R^{(3)}(\omega) \gg \chi_{NR}^{(3)}(\omega)$, the cross term between the resonant and non-resonant components of Eq. (2) is sufficiently small compared to the resonant response that it can be neglected. In this limit, the CARS spectrum and the Raman spectrum will be nearly identical. We have verified this experimentally by examining the spectra of microscopic diamond samples (not shown) where the resonant reponse is overwhelmingly large. Secondly, we emphasize that spatial-spectral coupling is due exclusively to optical effects within the Rayleigh range of the microscope focus. In larger bulk samples, where the resonant molecules are uniformly distributed within an inhomogeneous medium whose extent is greater than the Rayleigh range, the Gouy phase term can be safely neglected since the Gouy phase shifts of the resonant and non-resonant components will be equal except at the interface between the two [21]. In these situations, the Raman spectrum will be retrieved faithfully by standard retrieval algorithms.

In general, spatial-spectral coupling will inevitably make Raman spectrum retrieval more complicated. In the regime where these effects can be safely neglected, CARS will still occupy a key place in many nonlinear imaging applications. Moreover, as was demonstrated by the retrieval Raman data in Fig. 3(c), once the retrieval algorithm includes the spatial-spectral coupling, it can still reliably recover the vibrational Raman spectra from the sample. Consequently, it may be possible to resolve this issue entirely if retrieval algorithms are modified to calculate

#189626 - $15.00 USD Received 30 Apr 2013; revised 7 Jun 2013; accepted 9 Jun 2013; published 19 Jun 2013

$\chi^{(3)}(\omega)$ via Eq. (2) rather than Eq. (1). In addition, we note that such efforts may provide a novel route to significantly enhanced axial resolution, if the position of the emitter within the laser focus can be elucidated from the relative phase. For example, the nanometer-scale axial displacements of a cell membrane component or other small object within the laser focal volume could be monitored in real time by fitting the phase shift variations in the retrieved Raman spectrum, as implicitly suggested by Fig. 5. We are currently investigating such super-resolution strategies for CARS microscopy.

Acknowledgments

The authors acknowledge many useful discussions with Adrian F. Pegoraro (Harvard) and Rune Lausten (NRC). We also thank Benjamin J. Sussman (NRC) for discussions on phase retrieval and acknowledge financial support from the Natural Sciences and Engineering Research Council of Canada, Ontario Ministry of Research and Innovation, Canada Research Chairs program, Canada Foundation for Innovation and Mprime NCE Strategic Postdoctoral Fellowship program. We thank Dr. Christopher Kingston (NRC) for technical Raman support. Computations were performed on the Southern Ontario Smart Computing Innovation Platform (SOSCIP) BlueGene/Q supercomputer located at the University of Toronto's SciNet HPC facility.

#189626 - $15.00 USD Received 30 Apr 2013; revised 7 Jun 2013; accepted 9 Jun 2013; published 19 Jun 2013